

Received 3 February 2023, accepted 19 February 2023, date of publication 22 February 2023, date of current version 27 February 2023.

Digital Object Identifier 10.1109/ACCESS.2023.3247967



RESEARCH ARTICLE

Remote Sensing Image Dehazing Using Heterogeneous Atmospheric Light Prior

YUFENG HE[✉], (Member, IEEE), CUILI LI[✉], (Member, IEEE), AND XU LI[✉]

College of Information Engineering, Tarim University, Alxa 843300, China

Corresponding author: Cuili Li (licuili@taru.edu.cn)

This work was supported in part by the Natural Science Project of the Presidential Foundation, Tarim University, under Grant TDZKSS202140 and Grant TDZKSS202132; and in part by the Joint Funds of China Agricultural University and Tarim University under Grant ZNLH202103.

ABSTRACT Remote sensing images (RSIs) captured in haze weather will suffer from serious quality degradation with color distortion and contrast reduction, which creates numerous challenges for the utilization of RSIs. To address these issues, this paper proposes a novel haze removal algorithm, named HALP, for visible RSIs based on a heterogeneous atmospheric light prior and side window filter. HALP is comprised of two key components. Firstly, given the large imaging space of RSIs, the atmospheric light is treated as a globally non-uniform distribution instead of a global constant. Therefore, a simple and effective method for non-uniform atmospheric light estimation is presented, which utilizes the brightest pixel color in each local image patch as the atmospheric light of the local region. Secondly, a side window filter-based transmission estimation algorithm is proposed, which can effectively suppress the block effect in the transmission map caused by the large window of the minimum filter used in the dark channel algorithm. Experiments on both real-world and synthetic remote sensing haze images demonstrate the effectiveness of HALP. In terms of no-reference and full-reference image quality assessments, HALP yields excellent results, outperforming existing state-of-the-art algorithms, including physics-based and neural network-based methods. The visual comparison of dehazed results also shows that HALP can restore degraded RSIs with uneven haze, producing clear images with rich details and natural colors.

INDEX TERMS Dehazing, remote sensing image, heterogeneous atmospheric light, image restoration, dark channel.

I. INTRODUCTION

Haze is a highly common atmospheric phenomenon in nature, and its main ingredient is particles suspended in the atmosphere. When the scene radiance passes through the atmospheric medium and reaches the imaging device, it interacts with haze particles through absorption, reflection, and refraction. As a result, images acquired by remote sensing equipment are easily and adversely affected by haze, causing blurred edges and color distortions, and thus do not reflect accurate information about the ground surface, which reduces the utilization and value of RSIs. Images covered by haze still present some information about the ground surface, and it

The associate editor coordinating the review of this manuscript and approving it for publication was Geng-Ming Jiang[✉].

would be a huge waste of remote sensing resources if they were just discarded. Therefore, the necessary processing of haze-covered images to restore the full information in the image can effectively improve the availability and utilization of RSIs.

Most of the existing single image haze removal algorithms are designed for natural scene images taken near the ground. In the literature [1], [2], [3], [4], [5], the researchers proposed some priors based on observations, statistics, and hypotheses as clues to restore clear haze-free images. However, these algorithms cannot be effectively applied to remotely sensed images because there are distinct domain gaps between remotely sensed images and natural images, the most significant of which is that the distance of the remote sensing equipment from the observed object is much greater than

the depth of the ground-captured images, which makes RSIs more degraded by haze than natural images. Secondly, the RSI is a top view, and the spatial scope of the image is greatly larger than the scene spatial extent of the ground image. These differences make the atmospheric scattering model, widely used for natural image dehazing, not an accurate description of the physical process of remote sensing haze image degradation.

Considering the characteristics of remotely sensed imaging, researchers proposed dehazing algorithms for RSIs [6], [7], [8], [9], [10], [11]. They either proposed some new priors applicable to remotely sensed images or modified the existing prior derived from natural images to suit remote sensing scenes. Although these methods are conscious of the existence of differences between remotely sensed and natural images, they only consider the impact of these differences on the applicability of the haze prior and ignore the impact of these differences on the fundamental atmospheric scattering model, which is widely used for degraded image restoration. The atmospheric scattering model is a simplified ideal model that models the ambient light in the atmosphere as a global constant. This setting is reasonable for a natural image due to the limited space of the imaging scene. While it is not a good idea for RSIs to set the atmospheric ambient light as a global constant because the imaging space of RSIs is extremely wide. Based on this motivation, we modify the atmospheric scattering model so that it can cope with the RSI haze removal problem.

In addition to the traditional image-restore-based dehazing algorithms, more and more researchers turn their attention to emerging deep learning techniques and propose various effective methods for haze removal based on convolutional neural networks (CNNs) [12], [13], [14], [15], [16], [17]. However, these learning-based algorithms also face some challenges. Firstly, deep neural network-based dehazing algorithms do not have convincing interpretations, and they tend to work adequately on specific datasets, yet the generalization to cross-domain datasets results in a dramatic drop in performance. Secondly, CNN-based dehazing algorithms are hardware-dependent and require the deployment of additional hardware to the remote sensing space vehicle, significantly increasing the cost of the applications. Finally, deep learning-based methods require a large amount of training data, especially in supervised learning. The training of the dehazing models requires paired samples of hazy and haze-free images captured at the same time and same scene, which is extremely difficult to collect. Therefore, researchers are forced to train the models using synthetic images as training data [18], [19], [20]. However, there will be unavoidable differences between synthetic and real-world haze images.

In this paper, we propose a heterogeneous atmospheric light prior by analyzing the imaging specificity of RSIs, that is, atmospheric light in RSIs is not globally uniform and cannot be simply considered as a global constant. Meanwhile, we combine the global atmospheric light estimation method introduced in Tan's work [21] with our heterogeneous

atmospheric light prior, and propose a simple and effective heterogeneous atmospheric light estimation algorithm, which uses the image blocking strategy to compute the local atmospheric light value for each patch of image and then uses guided filter to get a global smooth nonuniform atmospheric light map. In addition, we use an improved dark channel algorithm to calculate the transmission map, which is another key factor for hazy image restoration. We find that the original dark channel dehazing algorithm is highly sensitive to the parameter of the patch size used to compute the dark channel. A small patch will lead to dark channel prior failure and overestimate the haze concentration of the image, dimming the dehazed image, while a large patch will cause a serious blocking artifact in the transmission map, creating halos in the restored image. Moreover, the larger the patch size, the higher the computational complexity, which makes the algorithm difficult to deploy for applications with strong real-time requirements. Therefore, we use the side window filter instead of the minimum filter to efficiently compute the transmission map, and the excellent edge-preserving property of the side window filter can effectively suppress the halos in the dehazed results.

In order to validate our algorithm, extensive comparative experiments were conducted on real-world and synthetic remote sensing haze images, and quantitative and qualitative results demonstrated the effectiveness of the proposed HALP algorithm. It is worth mentioning that HALP also shows good results in natural image haze removal.

The main contributions of this paper can be summarized as follows:

- Firstly, we present a novel heterogeneous atmospheric light prior based on the imaging properties of remote sensing scenes, and modify the atmospheric scattering model according to this prior so that it can better deal with the restoration problem of the remote sensing haze images.
- Secondly, based on the global non-uniformity and smoothness of the atmospheric light, we propose a heterogeneous atmospheric light estimation algorithm using the image blocking strategy.
- Finally, by analyzing the edge blurring problem of the transmission in the original dark channel algorithm, we propose a simple and effective transmission calculation method based on a side window filter, and take the estimated transmission and the non-uniform atmospheric light into the modified atmospheric scattering equation to recover the clear and haze-free RSIs.

II. RELATED WORK

Human efforts in degraded haze image restoration have been made for a long time, and numerous excellent algorithms have been proposed successively. In this section, we will present a brief review of existing techniques for single image haze removal. It should be noted that many outstanding algorithms were initially designed for natural scene images, and only in recent years have dehazing techniques been developed

specifically for remote sensing scenes. The inherent differences between RSIs and natural scene images lead to weak compatibility between these two types of methods. Therefore, according to the development process of haze removal technology, we will review dehazing algorithms specifically for natural scenes and remote sensing scenes, respectively, which can be broadly divided into two categories: prior-based and deep-learning-based dehazing methods.

A. PRIOR-BASED DEHAZING METHODS

From the perspective of the physical imaging model of haze images, the prior-based methods restore the unknown depth information, atmospheric light, and clear haze-free image through a given hazy image, and thus such methods are also called physical-model-based methods. The physical model widely used in the restoration tasks of degraded images caused by bad weather is the atmospheric scattering model, which is an underdetermined equation when only a haze image is given but additional information is not available. Therefore, the priors derived from the observation, statistics, and assumptions of the haze image can be used as supplementary constraints to the model, allowing the equations to be solved to restore the haze-free images.

Tan [21] observed that haze-free images have higher contrast compared to hazy images and airlight varies smoothly in the whole image. Taking these observations as clues, he proposed a simple method to enhance the visibility of hazy images. He et al. [1] proposed the dark channel prior through the statistics of a large number of images, which is that the value of the minimum channel of the patches in a haze-free image is always close to 0, and then they used dark channel prior to estimate the transmission map of the haze image and removed haze according to the atmospheric scattering model. Fattal [2] presented the color-line method to remove haze based on the regularity that pixels of a local patch in natural images often exhibit a one-dimensional distribution. Berman et al. [5] proposed a no-local approach for single image dehazing based on the color line prior, which presupposes that the colors of a haze-free image can be well approximated by a few hundred distinct hues in RGB space. By statistical analysis of a large number of hazy images, Zhu et al. [3] found a positive correlation between haze density and depth of the image, as well as the difference between brightness and saturation, which is termed as color attenuation prior, and they removed haze using this prior. Bui et al. [4] constructed color ellipsoids to fit haze pixel clusters of the hazy image in RGB space and calculated transmission through color ellipsoid geometry. Using wavelet transforms and the mean vector L2-norm techniques, Khmag et al. [22] proposed the dehazing algorithm based on edge and texture preserving. In addition, Zhu et al. [23] and Zheng et al. [24] presented image fusion-based dehazing methods, respectively. These methods rely heavily on the robustness of corresponding rules, and they would perform badly in some real-world scenes where the assumption fails.

In addition, these methods are based on the statistics and assumptions of natural scene images, which are not well applicable to remotely sensed images.

Because of the shortcomings of the above methods, some researchers have tried to find the latent priors of remote sensing hazy images as supplementary constraints for dehazing. Xie et al. [6] discovered the relationship between the dark channel and saturation of RSIs and proposed a dehazing algorithm based on the dark channel-saturation prior. Pan et al. [7] deformed the atmospheric scattering model by adding a translation term, and then combined it with the dark channel prior to develop a new defogging algorithm. Xu et al. [8] proposed the concept of virtual depth for the physical model of remote sensing imaging and an iterative dehazing approach, which combines patch-wise and pixel-wise operators to get the dehazed results with better visibility. Li et al. [9] presented a two-stage algorithm using the sphere model improved dark channel prior and homomorphic filter for haze and thin cloud removal in RSIs. Liu et al. [10] regarded the haze as additive contamination, which can be represented by a haze thickness map, and then proposed a ground radiance suppressed haze thickness estimation method to calculate the haze distribution and remove haze. Zhu et al. [25] built a linear model for scene depth calculation of RSIs, estimated atmospheric light by corresponding scene depth, and got the transmission map using the haze-lines algorithm. Although these algorithms are designed specifically for remote sensing hazy images, they all follow the traditional atmospheric scattering model without fundamentally considering the differences in the degradation models between the remotely sensed images and natural images. Relatively, the range of imaging scenes in RSI is large, which no longer supports the assumption of global uniformity of atmospheric light in the idealized atmospheric scattering model.

B. DEEP-LEARNING-BASED DEHAZING METHODS

In recent years, emerging deep learning techniques have achieved satisfactory results on various challenging vision tasks, and various convolutional neural network (CNN) based methods have been proposed to deal with the restoration of hazy images. Cai et al. [12] designed the DehazeNet to estimate the transmission maps of natural haze images, in which a novel nonlinear activation function, the Bilateral Rectified Linear Unit (BReLU), was introduced. Similarly, Ren et al. [13] adopted a multi-scale convolutional neural network (MSCNN) to calculate the transmission map, in which a coarse-scale subnetwork is used to estimate the holistic transmission, and then a fine-scale subnetwork refines the previous results. Li et al. [14] and Chen et al. [17] proposed end-to-end haze removal networks, respectively, AOD-Net and GCANet, which learn the direct mapping between the degraded and original image without solving transmission and atmospheric light. Li et al. [26] and Liu et al. [27] incorporated the attention mechanism into the architecture of the neural network model and obtained excellent dehazing

results. Dong et al. [16] designed a multi-scale boosted dehazing network based on two principles, boosting and error feedback, which can successfully restore degraded natural scene images. Gu et al. [19] proposed a dense attention-enhanced encoder-decoder network, which can directly recover the corresponding clear results from remotely sensed hazy images, and they synthesized a large-scale hazy remote sensing dataset to train the model. For the problem that paired RSIs with and without haze are difficult to acquire, Hu et al. [20] and Mehta et al. [28] proposed two dehazing algorithms based on unsupervised learning. Similar to the previous study [13], Li et al. [29] presented a two-stage dehazing model, FCTF-Net, which is a first-coarse-then-fine neural network based on channel attention mechanism and residual learning.

While deep learning-based dehazing algorithms have shown promising results, they tend to rely heavily on training samples and perform poorly on cross-domain test images. Moreover, under the prevailing supervised learning framework, a large number of remotely sensed image pairs with and without haze are required for training models, which is difficult to collect, so most of the current algorithms based on deep learning use synthetic datasets to train the network. However, the distribution of synthetic haze is different from that of the real world. In addition, deep learning-based algorithms are difficult to deploy in real-time applications due to their hardware dependence and excessive computation.

III. THEORETICAL FOUNDATION

In this section, two significant theoretical foundations for single image haze removal, the atmospheric scattering model and the dark channel prior, will be briefly introduced.

A. ATMOSPHERIC SCATTERING MODEL

In haze weather, the irradiance reflected by scene objects passes through the atmospheric medium and reaches the imaging equipment, forming a hazy image, as shown in Fig. 1. In this process, two physical phenomena occur simultaneously: first, the absorption and scattering of the scene radiation by atmospheric particles attenuates the scene radiation

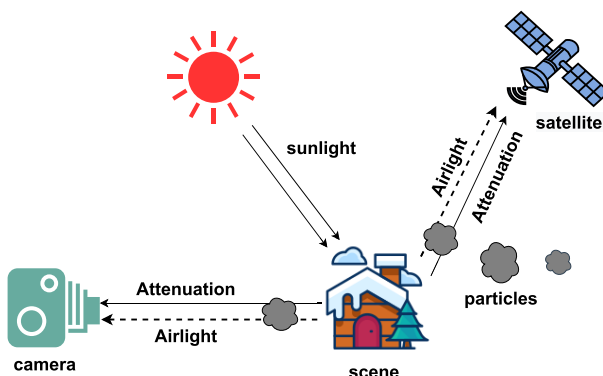


FIGURE 1. Illustration of the imaging process in haze weather. The solid line describes the propagation of the scene radiation, where the direct Attenuation occurs, and the dashed line shows the Airlight phenomenon.

along the line of sight, which is called direct attenuation; second, ambient light is also scattered into the propagation path of the scene radiation by particles suspended in the air, which is called airlight [30], [31]. The direct attenuation reduces the contrast and saturation of the image, while the airlight blurs the image and causes color distortion.

In the field of image restoration, the atmospheric scattering model is widely used to formulate the imaging process described above as follows [1], [5], [21], [30]:

$$I(x) = J(x)t(x) + A(1 - t(x)) \quad (1)$$

where I and J are haze image and the initial irradiance reflected from scene objects, respectively, and x is the pixel position. The symbol A denotes atmospheric ambient light, which is constant here, i.e., the model assumes that atmospheric illumination is uniformly distributed in global imaging space. The variable $t(x)$ represents the medium transmission, which measures the ratio between the received radiance through the atmospheric medium and the initial scene irradiance, so $t(x) \in [0, 1]$. The challenge of haze removal is to recover unknown J , A , and t simultaneously from a given degraded image I .

B. DARK CHANNEL PRIOR

According to the description in Section III-A, the image dehazing task is to solve the atmospheric scattering model, which is an underdetermined equation, so some additional constraints are needed to make the equation have a practical solution. The dark channel prior [1] is a strong supplementary constraint for the imaging model, providing a useful cue for calculating the transmission and the atmospheric light. It derives from the observation that the value of the minimum channel in a haze-free image patch invariably tends to 0, and this channel is called the dark channel that can be formulated as follows:

$$J^{dark}(x) = \min_{y \in \Omega(x)} \left(\min_{c \in \{r, g, b\}} J^c(y) \right) \quad (2)$$

where J^c and J^{dark} indicate the RGB color channels and the dark channel of the given image y , respectively. $\Omega(x)$ denotes

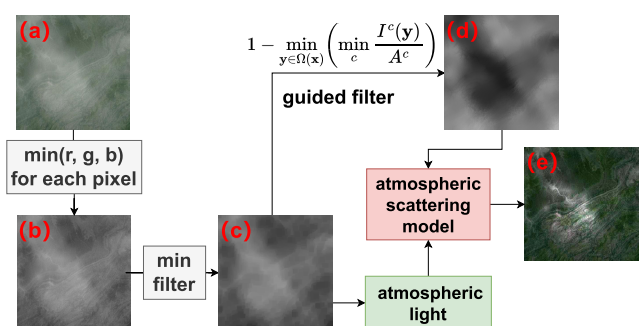


FIGURE 2. The calculation of the DCP algorithm [1]. (a) Hazy image; (b) Minimum channel of each pixel in (a); (c) Dark channel map calculated by a minimum filter on (b); (d) Transmission map refined by a guided filter; and (e) Dehazed result calculated by atmospheric scattering model.

an image patch whose center is located at x . Then J^{dark} approximates to zero when J is a haze-free image, as shown in column (c) of Fig. 2. Therefore, we can measure the haze intensity by the dark channel value of the hazy image and estimate the transmission by reformulating Eq. (1) and Eq.(2):

$$t(x) = 1 - \min_{y \in \Omega(x)} \left(\min_c \frac{I^c(y)}{A^c} \right). \quad (3)$$

The calculation flow of DCP method is shown in Fig. 2. For most hazy images, the DCP method produces satisfactory results. However, it may fail in some scenes where the dark channel prior is invalid. Furthermore, we also find that the dark channel prior is closely related to the size of the local patch used to calculate the dark channel.

IV. PROPOSED METHOD

In this section, we present in detail the three innovative contributions of the proposed HALP algorithm in turn. Firstly, we introduce the heterogeneous atmospheric light prior, and based on this prior, we improve the conventional atmospheric scattering model. Secondly, given the nonuniformity and smoothness of atmospheric light, we provide a detailed description of the proposed non-uniform atmospheric light estimation algorithm. Then, the defects of the transmission prediction in the dark channel dehazing method are analyzed, and an improved transmission map estimation algorithm based on the side window filter is proposed. Finally, the known non-uniform atmospheric light and transmission map are put into the heterogeneous atmospheric scattering model to calculate the haze-free image corresponding to the haze input.

A. NON-UNIFORM ATMOSPHERIC LIGHT ESTIMATION

The traditional atmospheric scattering model is proposed based on the assumption that the atmospheric light in the entire atmospheric space is globally homogeneous [30], [32]. It is just a simplified description of the atmospheric environment, which is much more complex in reality. The diversity of chemical composition of the cloud, fog, and haze, as well as the uneven and dynamic distribution of atmospheric particles, lead to different degrees of absorption, dispersion, and transmission of the light at different locations in the atmospheric space, which makes the ambient light in the atmosphere not evenly distributed. Due to the wide imaging space of RSIs, the inhomogeneous distribution of atmospheric light is more prominent. Based on this observation, we propose a non-uniform atmospheric light prior and reformulate the atmospheric scattering model as follows:

$$I(x) = J(x)t(x) + A(x)(1 - t(x)) \quad (4)$$

which is similar to the traditional atmospheric scattering model shown in Eq. (1) and inherits its notations' meaning. However, atmospheric light, denoted as $A(x)$ here, is no longer a global constant but a variable related to spatial

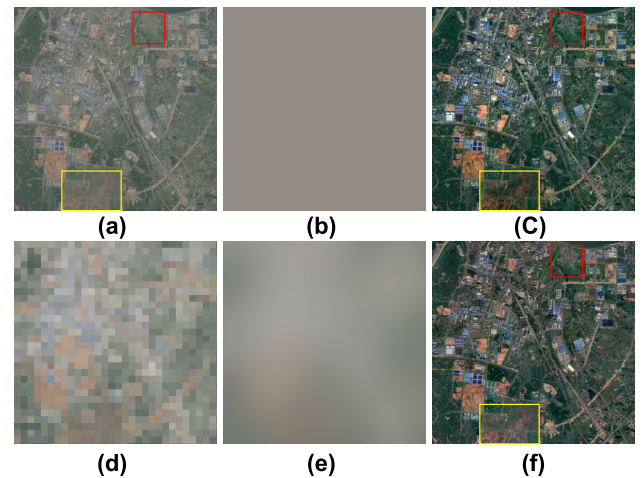


FIGURE 3. Uniform and non-uniform atmospheric light and their corresponding dehazing results. (a) Hazy input. (b) The global uniform atmospheric light calculated by DCP [1]. (c) Dehazed result by DCP. (d) The coarse atmospheric light calculated by our image patch strategy. (e) The non-uniform atmospheric light smoothed by the guided filter. (f) Dehazed result by our method.

location, which makes it difficult to apply the previous dehazing algorithms directly to this modified model.

Following the Tan's work [21], in hazy weather, sunlight is typically weak and can be ignored. The predominant imaging light source is atmospheric light, so the scene radiance can be described by

$$J(x) = R(x)A(x) \quad (5)$$

where $R(x)$ is the reflectance of the scene object, and $R(x) \leq 1$. Therefore, Eq. (4) can be rewritten as

$$I(x) = R(x)A(x)t(x) + A(x)(1 - t(x)) \quad (6)$$

$$= A(x)[1 + (R(x) - 1)t(x)] \quad (7)$$

Since $t(x) \geq 0$ and $R(x) \leq 1$, $I(x) \leq A(x)$. Approximately, we treat the maximum intensity of each image patch as the local atmospheric light. More specifically, we divide the hazy image into non-overlapping patches with a fixed-size window, then find the pixel with the largest intensity in each subpatch and take the color of this pixel as the local atmospheric light of the corresponding area. Therefore, the coarse non-uniform atmospheric light can be formulated as

$$A_{coarse}(x) = V2RGB(\max_{y \in \Omega(x)} (I^v(y))) \quad (8)$$

where x denotes the center of the local image patch $\Omega(x)$, y denotes pixels in the Ω , and $I^v(y)$ represents the v-channel in the HSV space of the pixel y . \max and $V2RGB$ are two functions, the former finds the maximum value, the latter converts the v-channel to RGB space referring to the given input, and A_{coarse} indicates the obtained coarse non-uniform atmospheric light.

The A_{coarse} calculated above has a severe block effect, while the distribution of ambient light is continuous, so we use a guided filter to smooth A_{coarse} to obtain the final non-uniform atmospheric light. Fig. 3 shows the atmospheric

light estimated by the dark channel algorithm and our method, respectively, as well as the corresponding restored haze-free images. The algorithm proposed in this paper can restore the haze-free image with higher visual quality. The areas marked by red and yellow boxes in the figure clearly show that the colors recovered by our method are more vivid and more precisely represent the different ground covers.

B. TRANSMISSION ESTIMATION ALGORITHM IMPROVED BY SIDE WINDOW FILTER

Another crucial factor in RSI dehazing problem is the estimation of the transmission map. He et al. [1] proposed the dark channel prior through the statistical analysis on a large number of hazy images, that is, the minimum color component of the local patch in a haze-free image approaches 0, as described in Eq. (2) in Section III-B. He et al. used the dark channel as a powerful clue to estimate the scene transmission. However, the dark channel is closely related to a key parameter, the patch size for calculation. If this parameter is too small, the algorithm will overestimate the haze level of the scene, making the dehazed image overly dark. In the extreme case, when this parameter is as small as 1, the dark channel map degrades to the minimum channel image, and the confidence of the dark channel prior decreases sharply, making the algorithm fail; While this parameter is very large, it will lead to significant block effects in the obtained transmission, which causes some artificial halos in the restored image, and a large patch size will also make the computational overhead of the method increase dramatically.

Therefore, to ensure the validity of the dark channel prior, the radius of the local patch for calculating the dark channel cannot be too small. At the same time, block effects in the dark channel map should be avoided so that the edge and structure information of the original image can be retained.

We further analyze the root cause of the halo in the dark channel map: the traditional minimum filter used to find the darkest pixel in the local image patch will cause the edge diffusion phenomenon on the sharp areas of the image, which becomes worse as the radius of the filter kernel increases. Therefore, inspired by existing research [33], we propose an improved dark channel map calculation method based on the side window filter. The operation of the side window filter and the edge diffusion phenomenon caused by the traditional filter are shown in Fig. 4(a), where there is a vertical edge line, and the red and blue matrices are the traditional minimum filter and the side window minimum filter with 3×3 filter kernel, respectively. In the former filter, all the nine elements covered by the filter kernel are involved in the calculation, i.e., the region filled in red, so the minimum filtering result of the current anchor is 1, showing the diffusion of the edge contour. While in the latter case, the filter uses only the side area where the anchor is located for calculation, i.e., the blue-filled region, so the result of the current anchor is 249, thus preventing diffusion cross the edges. For the side window filter to match diverse edges adaptively, we follow the strategy in literature [33] and summarize the edges into

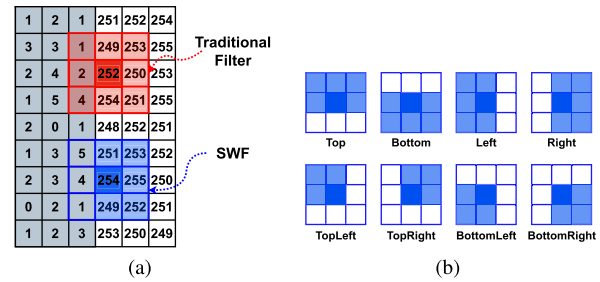


FIGURE 4. Illustration of the side window filter. (a) Difference between the traditional filter and the side window filter (abbreviated as ‘‘SWF’’). (b) The kernels of the side window filter for matching various edges.

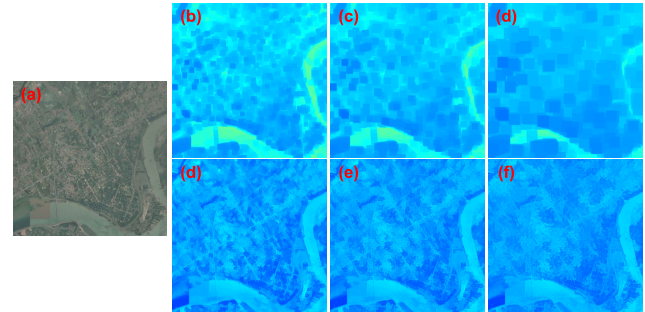


FIGURE 5. Dark channel maps obtained by DCP and the proposed HALP algorithm using different patch size. (a) is input hazy image. (b), (c) and (d) are dark channel maps calculated by DCP using 15×15 , 21×21 and 35×35 patch size, respectively. (e), (f) and (g) are our results using the same patch size with (b), (c) and (d), respectively. For better view, pseudo-color images are displayed instead of the original single-channel dark channel maps.

eight classes shown in Fig. 4(b) where the top four classes are line templates and the bottom four classes are corner templates.

We can calculate the transmission map by

$$t(x) = 1 - SWF_{y \in \Omega(x)} \left(\min_c \frac{I^c(y)}{A^c(y)} \right). \quad (9)$$

where SWF indicates the side window filter and the other letters represent the same concepts as Eq. (3).

Fig. 5 shows the dark channel maps obtained by DCP and our method using different patch sizes. It can be seen that He’s results arise significant block effects with the increase in patch size, while the edges and structure of the image are nicely preserved by our method

C. HAZE REMOVAL FOR REMOTE SENSING IMAGE

Fig. 6 depicts the flow of the proposed HALP algorithm: the single remote sensing image, as well as the non-uniform atmospheric light obtained in Section IV-A, and the transmission calculated in Section IV-B, are simultaneously brought into the heterogeneous atmospheric scattering model to restore the final haze-free image, which can be described as

$$J(x) = \frac{I(x) - A(x)}{\max(t(x), t_0)} + A(x) \quad (10)$$

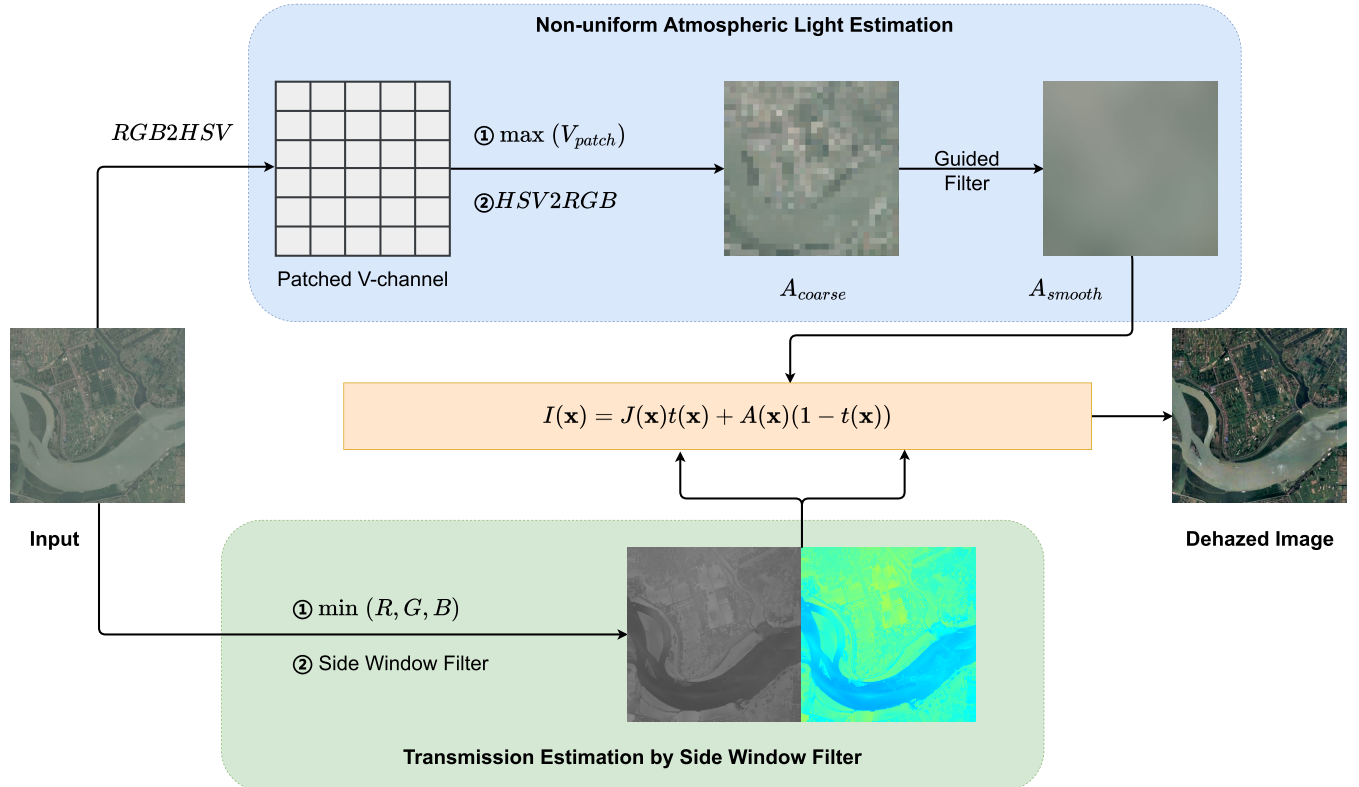


FIGURE 6. Illustration of the proposed HALP. The transmission map is a single-channel image, and its pseudo-color image is supplemented for a better view here.

where t_0 represents the lower limit of transmission, which is used to suppress the noise of $J(x)$ when $t(x)$ is extremely small, and we let $t_0 = 0.1$ here.

V. EXPERIMENTS

In this section, to fairly verify the effectiveness of the proposed algorithm, we qualitatively and quantitatively compared the dehazing performance of our method with several state of the arts, including HazeLine [5], IDE [34], AOD [14], GDN [27], AHR [6], DHIM [7], and SMIDCP [9], where HazeLine and IDE are physical-model-based dehazing methods for natural images, AOD and GDN are emerging technologies based on deep learning, while the last three algorithms are specially proposed for RSIs. The source codes of all compared algorithms are released by the original authors on their official websites, and we execute these methods directly without any extra modifications. Comparative experiments were performed both on real-world and synthetic remote sensing hazy images. The source code of the HALP is available on <https://github.com/foreverfruit/HALP>

A. QUALITATIVE EXPERIMENTS

At present, there is no publicly available real-world dataset for remote sensing dehazing. Therefore, we constructed a Real-world Remote Sensing Haze Image Dataset (RRSHID), which consists of 277 haze-contaminated images manually selected from two classical remote sensing datasets, AID [35]

and DIOR [36]. 150 images with the resolution of 600×600 are collected from the AID dataset, and the remaining 127 images with the resolution of 800×800 are from the DIOR dataset. More details of the RRSRID dataset will be released in the official code repository. To comprehensively compare the dehazing effects of each method, three experiments were conducted on images with different haze distributions, different color characteristics, and different scenes.

1) HAZE REMOVAL FOR DIFFERENT HAZE DISTRIBUTED IMAGES

The performance on RSIs with different haze distributions is an important evaluation for dehazing algorithms. Fig. 7 shows the comparison of the dehazed results of different methods on RSIs with homogeneous haze. It can be seen that AHR and DHIM methods fail to restore the color of the bare ground, raising dim blocks in the lower left corner of the first test sample. Although the AOD algorithm can effectively remove haze, the results of both images are dark with low color saturation, while the GDN, the other method based on deep learning, can not dehaze properly for given RSIs, leaving an obvious white veil of haze. The SMIDCP and IDE methods can slightly alleviate the haze problem, but they both suffer from color distortion, the former mistakenly restores the water back to green for the top image, while the latter turns it to bright blue. The results of HazeLine and HALP method, by contrast, have a better visual effect.

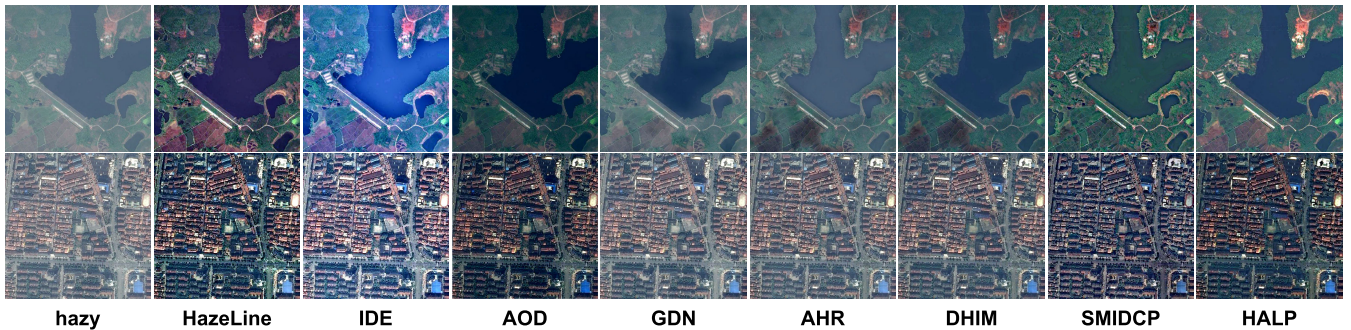


FIGURE 7. Dehazed results by different methods on real-world RSIs with homogeneous haze. The columns from left to right are the haze input, and the dehazed results of HazeLine [5], IDE [34], AOD [14], GDN [27], AHR [6], DHIM [7], SMIDCP [9], and the proposed HALP.

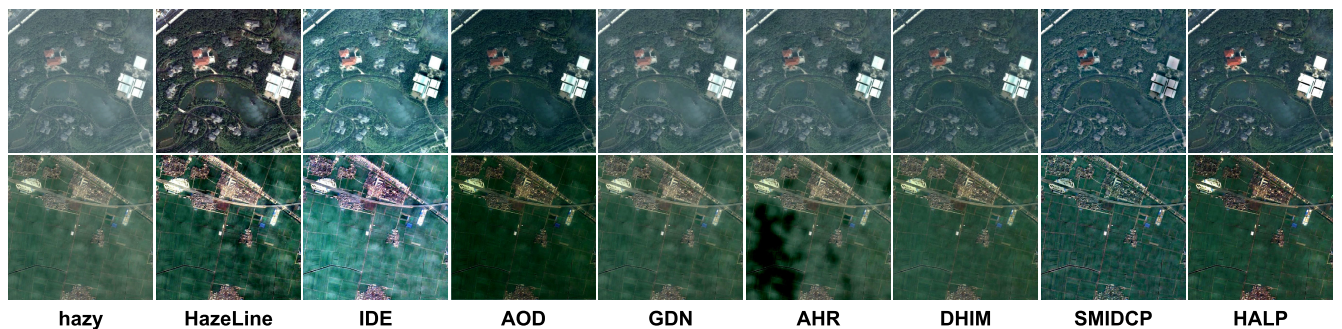


FIGURE 8. Dehazed results by different methods on real-world RSIs with heterogeneous haze. The columns from left to right are the haze input, and the dehazed results of HazeLine [5], IDE [34], AOD [14], GDN [27], AHR [6], DHIM [7], SMIDCP [9], and the proposed HALP.

For remote sensing images with heterogeneous haze, the results of each algorithm vary greatly, as shown in Fig. 8. The algorithms of AOD, GDN, and AHR fail to obtain clear and haze-free results. Moreover, IDE has a serious overexposure problem. The restored results of SMIDCP and HazeLine methods remain a large amount of haze. DHIM and the presented HALP method can effectively remove haze, and results of HALP are much more satisfying in color.

The test images in Fig. 9 are four RSIs covered by dense haze. SMIDCP algorithm over-sharpenes the restored images and produces inappropriate colors. The IDE algorithm gets favorable dehazing results on the first two test samples, but the last two images show color shifts. The results of AOD and DHIM algorithms are too dark, while GDN and AHR dehaze incompletely. Similar to Fig. 7, HALP and HazeLine still have superior fog removal ability in the case of thick haze.

2) HAZE REMOVAL FOR IMAGES WITH DIFFERENT COLORS

Color has a significant effect on the performance of the dehazing algorithm, and it is worthwhile to evaluate the algorithm's recovery ability for scenes with different colors. We test all the compared methods on images with monotonous color, rich colors, and local white, respectively.

As shown in Fig. 10 and Fig. 11, HazeLine and IDE algorithms have good dehazing performance on rich color images, but serious overexposure likely occurs on scenes with monotonous color. In contrast, SMIDCP cannot restore

images well on color-rich scenes, as shown in the 8th column of Fig. 11. The AOD method consistently produces disappointing results with low saturation and low brightness. The methods of GDN, AHR, and DHIM do not work in some test samples, such as the last test image in Fig. 10, and sometimes, AHR even generates unexpected black blocks on monotonous color scenes. HALP algorithm restores the light and darkness of the scene successfully and obtains clear images with high visual quality.

The local white regions in haze images may lead to the incorrect estimation of the atmospheric light by some dehazing algorithms, resulting in unsatisfactory restored images, as shown in the outputs of AOD, GDN, AHR, DHIM, and SMIDCP algorithms in Fig. 12. Since HALP method employs a local strategy to calculate global non-uniform atmospheric light, it works well even if the input has local white areas.

3) HAZE REMOVAL FOR IMAGES OF DIFFERENT SCENES

To evaluate the generalization of dehazing algorithms for different scenes, we also select remote sensing images of eight common scenes from the previously mentioned RRSRID, which are viaduct, river, park, mountain, residence, bridge, airport, and school. The visual comparisons of dehazed results are shown in Fig. 13.

Similar to the previous experimental phenomenon, the results of the IDE algorithm show oversaturation in different scenes, while AOD's show insufficient color saturation. GDN, AHR, and DHIM algorithms are not always

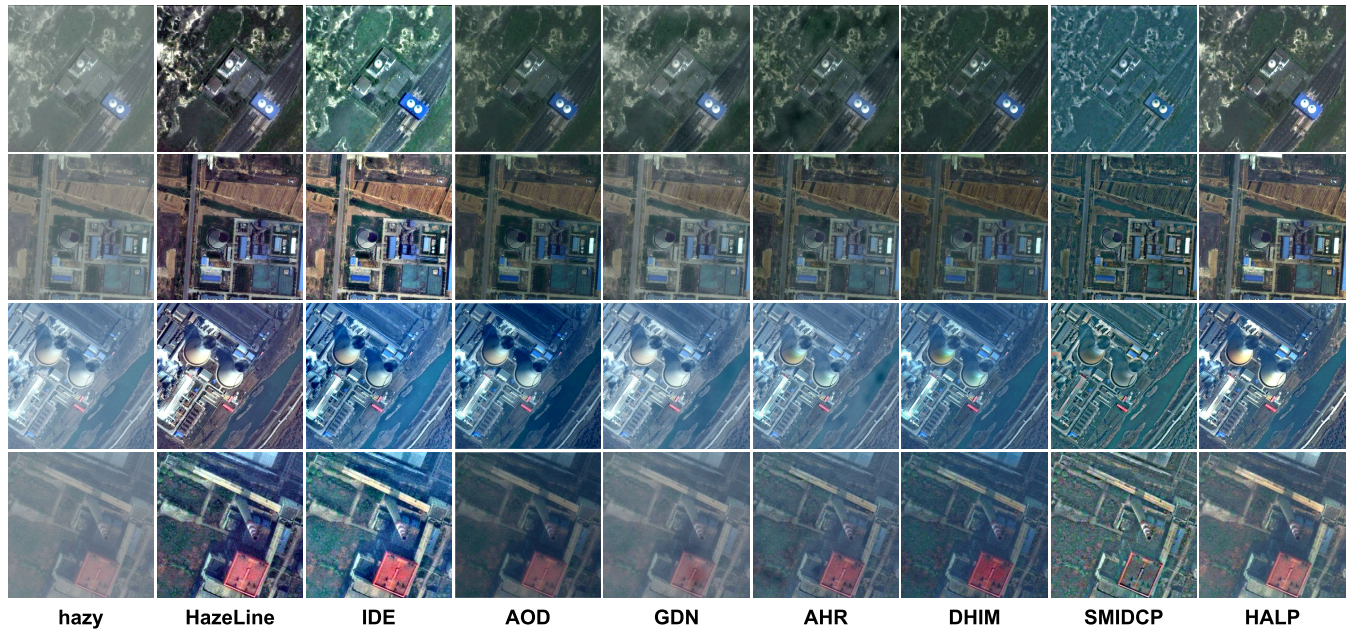


FIGURE 9. Dehazed results by different methods on real-world RSIs with thick haze. The columns from left to right are the haze input, and the dehazed results of HazeLine [5], IDE [34], AOD [14], GDN [27], AHR [6], DHIM [7], SMIDCP [9], and the proposed HALP.

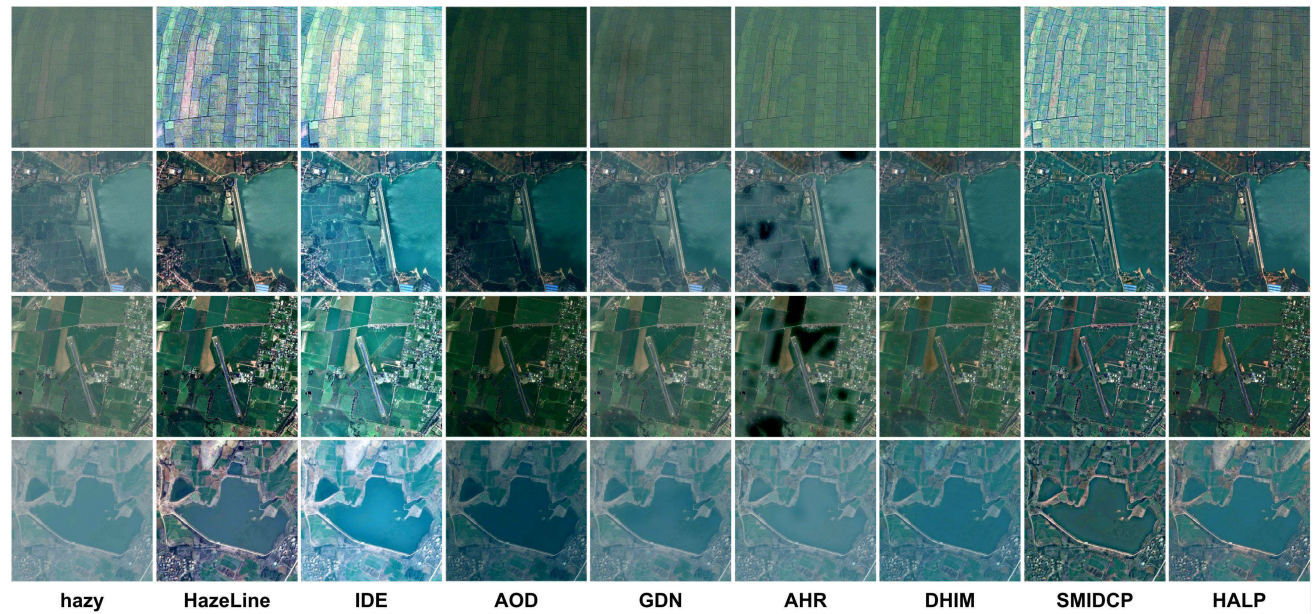


FIGURE 10. Dehazed results by different methods on real-world RSIs with monotonous color. The columns from left to right are the haze input, and the dehazed results of HazeLine [5], IDE [34], AOD [14], GDN [27], AHR [6], DHIM [7], SMIDCP [9], and the proposed HALP.

effective and tend to leave some of the haze. While SMIDCP often suffers from color distortion. Both HazeLine and HALP have good dehazing performance for various scenes, and our results have richer texture details and more natural colors.

B. QUANTITATIVE EXPERIMENTS

1) BLIND IMAGE QUALITY ASSESSMENTS FOR REAL-WORLD RSI DEHAZING

In addition to the qualitative visual comparison, we also conduct a quantitative experiment on the effect of various

algorithms dehazing on real-world remotely sensed haze images. In this experiment, we adopt four widely used blind image quality assessments (BIQAs), which are NIQE [39], BRISQUE [40], FADE [41], and HDMHA [42]. NIQE calculates the perceptual quality score of the input image by comparing it to a default model trained using natural scene images. BRISQUE compares the target image to a ready model computed from natural images with similar distortions to estimate a corresponding no-reference image quality score. Therefore these two metrics are common-used in various

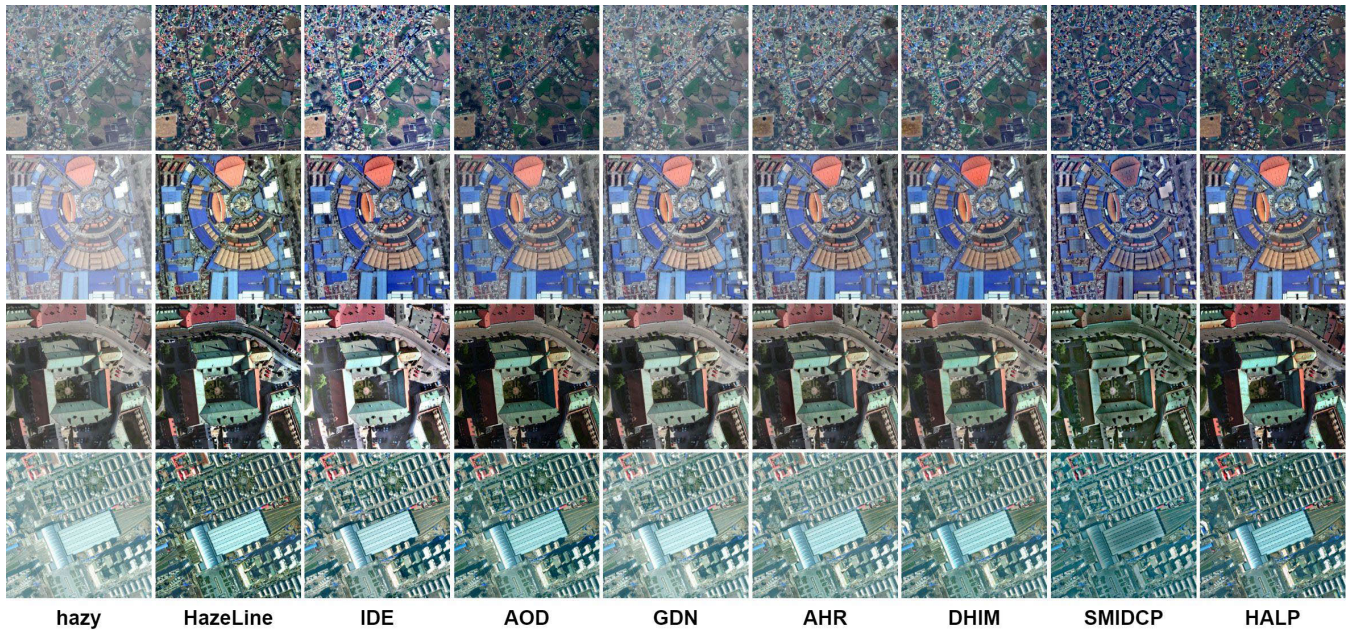


FIGURE 11. Dehazed results by different methods on real-world RSIs with rich colors. The columns from left to right are the haze input, and the dehazed results of HazeLine [5], IDE [34], AOD [14], GDN [27], AHR [6], DHIM [7], SMIDCP [9], and the proposed HALP.

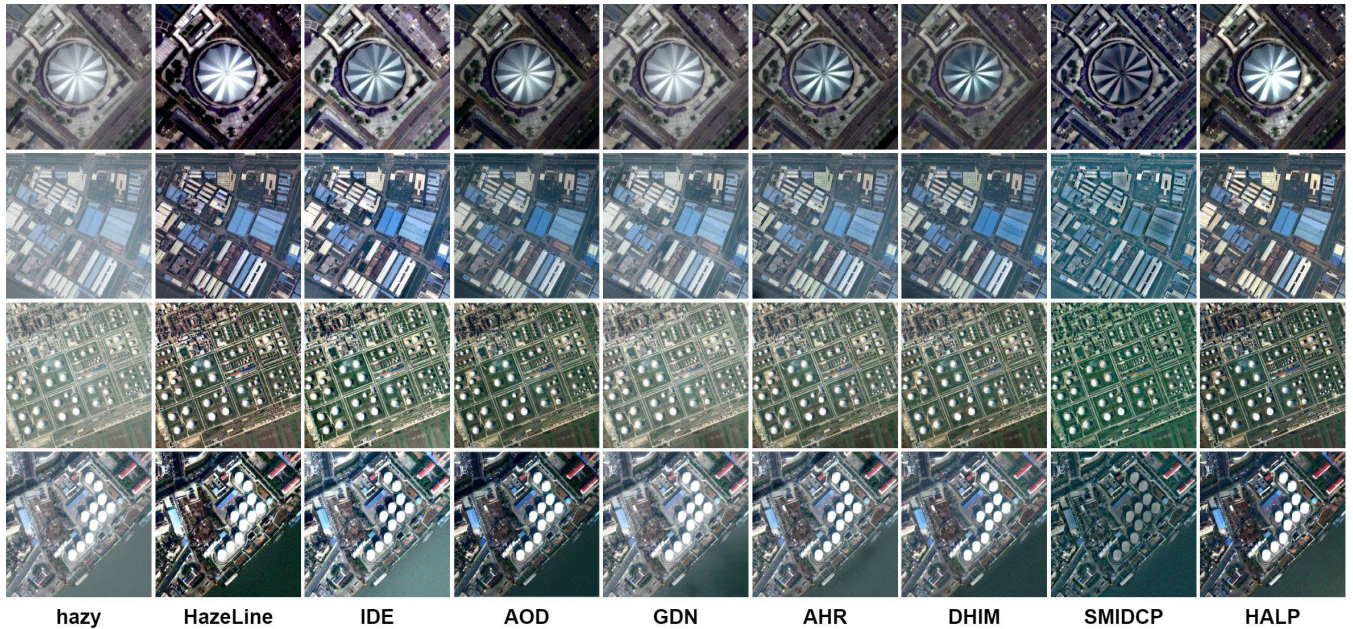


FIGURE 12. Dehazed results by different methods on real-world RSIs with local white patches. The columns from left to right are the haze input, and the dehazed results of HazeLine [5], IDE [34], AOD [14], GDN [27], AHR [6], DHIM [7], SMIDCP [9], and the proposed HALP.

image restoration tasks. The smaller scores of NIQE and BRISQUE indicate the better perceptual quality of the given image. While FADE and HDMHA are specially designed for image haze removal task and they can measure the haze density contained in images, and they represent the lower perceptual haze density by the lower values.

We execute all comparison algorithms to remove haze for all test images in the RRSRID dataset, and then calculate the

average scores of the dehazed results by each method using four BIQAs mentioned above, as shown in Table 1. For both the naturalness image perceptual quality assessments, NIQE and BRISQUE, our proposed algorithm gets the best scores, and the BRISUQE score is much better than the second-best score by IDE. It indicates that our dehazed results match the characteristics of natural images adequately and have less distortions. Meanwhile, our method has competitive haze

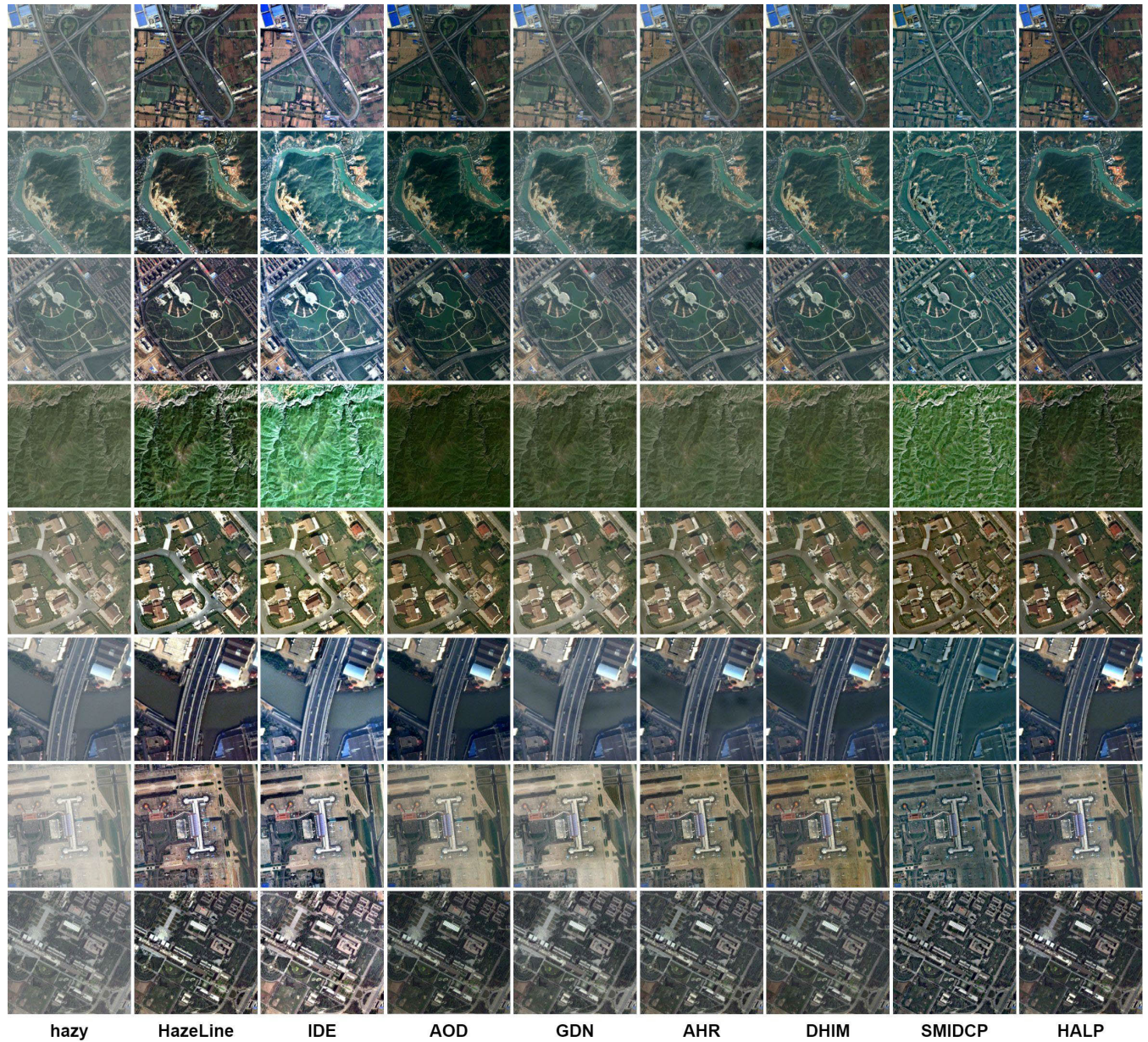


FIGURE 13. Dehazed results by different methods on real-world RSIs with various scenes, which are viaduct, river, park, mountain, residence, bridge, airport, and school from top to bottom. The columns from left to right are the haze input, and the dehazed results of HazeLine [5], IDE [34], AOD [14], GDN [27], AHR [6], DHIM [7], SMIDCP [9], and the proposed HALP.

TABLE 1. No-reference assessment scores of comparison methods dehazing on RRSHID dataset. Texts in red, blue, and cyan indicate the best, the second-best, and the third-best performance, respectively.

	HazeLine[5]	IDE[34]	AOD[14]	GDN[27]	AHR[6]	DHIM[7]	SMIDCP[9]	HALP
NIQE	3.654	3.659	3.467	3.479	3.511	3.497	3.764	3.466
BRISQUE	32.644	31.973	32.206	33.142	33.407	33.505	32.564	28.751
FADE	0.262	0.291	0.318	0.620	0.467	0.442	0.229	0.273
HDMIHA	0.045	0.084	0.029	0.171	0.028	0.020	0.007	0.017

density scores, and its HDMIHA score and FADE score rank 2nd and 3rd among all tested state of the arts, respectively.

It should be noted that although SMIDCP obtains the best HDMIHA and FADE scores, its over-processing makes the

TABLE 2. Full-reference assessment scores of comparison methods dehazing on synthetic remote sensing image datasets [37], [38]. ‘Haze1k-TN’, ‘Haze1k-M’ and ‘Haze1k-TK’ denote the thin, moderate and thick subset of the Haze1k dataset, respectively. ↑ means the better performance with the higher value, while ↓ means the opposite case. Texts in red, blue, and cyan indicate the best, the second-best, and the third-best performance, respectively.

	IQA	HazeLine[5]	IDE[34]	AOD[14]	GDN[27]	AHR[6]	DHIM[7]	SMIDCP[9]	HALP
Haze1k-TN	PSNR↑	13.921	18.587	19.196	14.799	18.838	19.445	13.639	19.785
	SSIM↑	0.738	0.889	0.892	0.834	0.893	0.891	0.824	0.899
	CIEDE2000↓	15.895	9.350	9.946	14.053	10.165	9.829	16.750	8.473
Haze1k-M	PSNR↑	15.454	16.920	17.891	14.918	18.489	19.916	15.990	18.858
	SSIM↑	0.771	0.879	0.884	0.852	0.910	0.917	0.856	0.909
	CIEDE2000↓	15.454	11.746	12.460	14.716	11.754	10.909	13.895	11.068
Haze1k-TK	PSNR↑	16.365	13.463	11.702	10.784	15.548	16.595	14.956	16.174
	SSIM↑	0.817	0.756	0.676	0.654	0.802	0.810	0.777	0.808
	CIEDE2000↓	12.793	14.886	19.836	22.021	15.959	15.273	15.519	12.202
RICE	PSNR↑	17.058	13.730	14.987	19.411	20.910	19.240	16.573	20.911
	SSIM↑	0.750	0.696	0.778	0.902	0.933	0.882	0.721	0.926
	CIEDE2000↓	14.888	22.380	16.543	11.063	8.478	11.167	17.862	10.978

recovered images have a lot of noise and distortions, so its perceptual quality evaluation is not satisfactory, for example, the worst NIQE score.

2) FULL-REFERENCE ASSESSMENTS FOR SYNTHETIC RSI DEHAZING

Besides the blind reference assessments above, we use full-reference IQAs to quantitatively and comprehensively evaluate the dehazing performance of all compared state-of-the-art algorithms. In this experiment, datasets Haze1k [37] and RICE [38] are used. Haze1k contains 1200 pairs of RGB remote sensing images with and without haze, among which the haze-free images are obtained by GF-2 satellite, and the corresponding hazy images are synthesized by the atmospheric scattering model. According to the density of the haze in samples, Haze1k is divided into three subsets, Haze1k-Thin, Haze1k-Moderate, and Haze1k-Thick, and each subset is further divided into test set, training set, and verification set. All comparison methods dehaze on test sets of these three subsets. By setting whether to display the cloud layer in Google Earth, Lin et al. [38] acquired 500 pairs of remote sensing images with and without haze, which constituted the RICE dataset.

We employ three widely used full-reference IQAs, the peak signal to noise ratio (PSNR), the structural similarity index (SSIM) [43], and CIEDE2000, to compare the restoration effectiveness of dehazing methods on the four datasets mentioned above. The PSNR evaluates the difference between the target image and the reference image pixel by pixel in terms of signal and noise, and a higher PSNR score represents better image restoration performance. The SSIM assesses the image quality from the brightness, contrast, and structure of the given paired images, and its value is between 0 and 1. The larger the SSIM value, the higher the similarity between the restored image and the original clear image.

While CIEDE2000 measures the color difference between two images, the smaller value means fewer color distortions in the dehazed image. All evaluation results are shown in Table 2.

SMIDCP suffers from severe color distortion on all four datasets, resulting in high CIEDE2000 scores. The IDE algorithm, due to its strategy of image exposure enhancement, leads to color instability in its dehazed images, so it has good color recovery on Haze1K, but over-enhances on RICE causing the worst CIEDE2000 value. The performance of the remaining comparison algorithms depends on the data distribution and varies greatly with different datasets. While the proposed HALP algorithm achieves promising evaluation results on all four datasets, indicating that HALP can restore the clear image well from the given remotely sensed haze image, and it creates gorgeous colors with little distortion and gets high visual perceptual quality.

VI. DISCUSSION

In this section, we first conducted a set of ablation experiments to quantitatively evaluate the contributions of each component of the proposed HALP algorithm to the dehazing performance. Second, we compared the execution efficiency of different dehazing algorithms on RSIs of three different resolutions, and discussed the relationship between the kernel size of the introduced side window filter and the performance of the HALP algorithm. Then, we further verified the effectiveness of the HALP by visual comparison of the intermediate results in dehazing. Finally, we tried to dehaze for natural scene images using the HALP method to explore the compatibility of its application scenes.

A. ABLATION STUDY

Similar to the traditional physical model-based dehazing algorithms, the key steps of the proposed HALP are atmospheric light and transmission map estimations. These

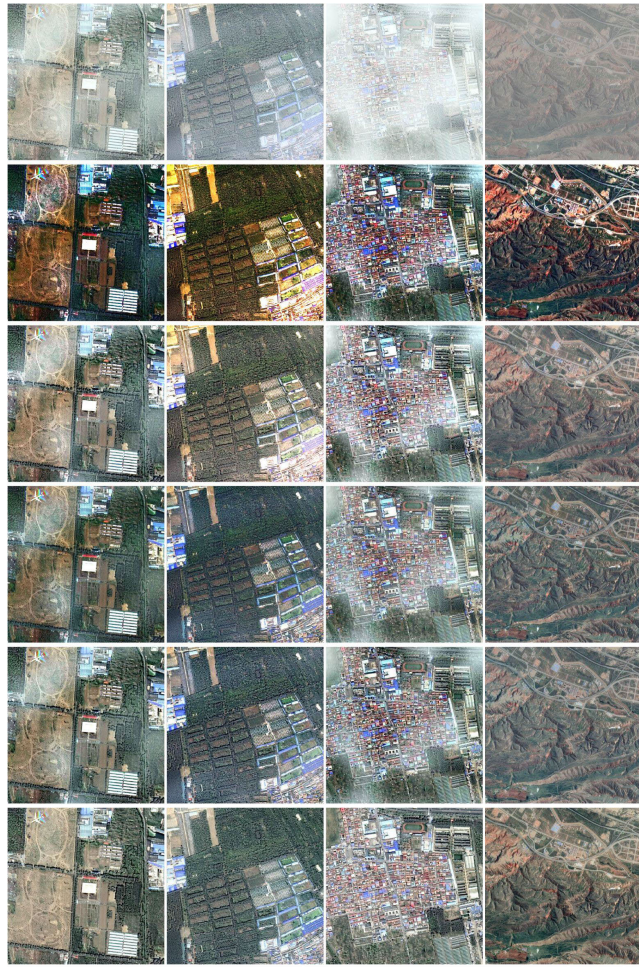


FIGURE 14. From top to bottom, images in each row are (1) hazy inputs, restored images by (2) the CEP [4], (3) $CEP+T_{HALP}$, (4) $CEP+A_{HALP}$, and (5) the proposed HALP algorithm, and (6) corresponding haze-free ground truths, respectively. The four haze images are samples in the RICE dataset [38] and the thin, moderate, and thick subset of the Haze1k dataset [37].

two parts are independent, so they can be split and labeled as A_{HALP} and T_{HALP} , respectively. We chose another acclaimed physical model-based dehazing algorithm, CEP [4], as the baseline, and replaced the computational procedures of the atmospheric light and transmission in the CEP with A_{HALP} and T_{HALP} respectively, resulting in two new algorithm variants (denoted as $CEP+A_{HALP}$ and $CEP+T_{HALP}$). We tested these methods on datasets Haze1k and RICE mentioned in Section III, and adopted full-reference assessments to quantitatively evaluate the effectiveness of the proposed atmospheric light and transmission estimation techniques.

The quantitative experimental results are shown in Table 3. On all the tested datasets, the scores of the three full-reference assessments consistently show that both A_{HALP} and T_{HALP} proposed in this paper can significantly improve the haze removal performance of the CEP algorithm. When A_{HALP} and T_{HALP} are used simultaneously (i.e. HALP method), the dehaze effect can be further improved. The visual comparison results are shown in Fig. 14. The images recovered by the

TABLE 3. Quantitative results of the ablation study. The meanings of the symbols in this table are the same as those in Table 2.

Dataset	Methods	PSNR↑	SSIM↑	CIEDE2000↓
Haze1k-TN	CEP[4]	14.107	0.682	20.745
	$CEP+T_{HALP}$	19.449	0.897	8.593
	$CEP+A_{HALP}$	17.779	0.857	11.076
	HALP	20.894	0.928	10.805
Haze1k-M	CEP[4]	13.083	0.684	20.046
	$CEP+T_{HALP}$	18.216	0.902	10.685
	$CEP+A_{HALP}$	18.198	0.879	12.529
	HALP	18.858	0.909	11.068
Haze1k-TK	CEP[4]	15.089	0.773	14.967
	$CEP+T_{HALP}$	15.340	0.801	12.835
	$CEP+A_{HALP}$	15.959	0.800	12.309
	HALP	16.174	0.808	12.202
RICE	CEP[4]	14.107	0.682	20.745
	$CEP+T_{HALP}$	19.954	0.914	11.751
	$CEP+A_{HALP}$	20.013	0.911	11.805
	HALP	20.911	0.926	10.978

original CEP algorithm suffer from color distortion, while the proposed techniques can effectively eliminate this problem and generate clear results close to the original haze-free inputs.

B. COMPUTATIONAL EFFICIENCY

In addition to dehazing effectiveness, the execution efficiency of the algorithm is also an essential factor for its wide application. Here we compare the average runtime of different algorithms. All of the algorithms run on the same computer, which is equipped with Intel(R) Core(TM) i7-10700 CPU, 32GB RAM, and NVIDIA GeForce RTX 3090 GPU. All methods are tested on Matlab R2020a, except for AOD and GDN, which are implemented using the Pytorch framework. We collect 100 haze remote sensing images with resolutions of 256×256 , 512×512 , and 1024×1024 , respectively, and then evaluate the average runtime for each algorithm to process these images. It should be noted that we test the runtime of the neural-network-based AOD and GDN algorithms both on CPU and GPU for a fair comparison. In our method, the image needs to be divided into patches when calculating atmospheric light. Therefore, we calculate the execution efficiency with different patch sizes (17×17 , 37×37 , and 57×57 , respectively).

As shown in Table 4, HazeLine and IDE have high computational overhead and are difficult to deploy in some applications with real-time response requirements. The runtime of the deep learning-based method is highly related to the complexity of the network structure. AOD is a lightweight model, so its computation overhead is quite low, while the network of GDN is complex and it needs GPU acceleration for low computation latency. Fig. 15 depicts the processing time of different algorithms as the input image resolution increases. It shows that AHR and SMIDCP can process tiny-size images quickly, but their computation time increases significantly when the resolution increases. In contrast, DHIM and HALP

TABLE 4. Average processing time of different algorithms dehazing for 100 images with three different resolutions. ‘CPU’ indicates that the neural network-based methods execute only on CPU without hardware acceleration, while ‘GPU’ indicates the opposite case. ‘PSA’ represents the patch size parameter used in the calculation of the atmospheric light.

	256 × 256	512 × 512	1024 × 1024
HazeLine[5]	1.525	2.376	5.048
IDE[34]	0.144	0.858	3.844
AHR[6]	0.063	0.340	1.589
DHIM[7]	0.012	0.069	0.315
SMIDCP[9]	0.121	0.350	1.424
AOD (CPU)[14]	0.062	0.242	0.986
GDN (CPU)[27]	0.620	2.551	10.141
AOD (GPU)[14]	0.002	0.007	0.030
GDN (GPU)[27]	0.020	0.041	0.189
HALP (PSA=17)	0.050	0.138	0.465
HALP (PSA=37)	0.151	0.248	0.609
HALP (PSA=57)	0.200	0.447	0.853

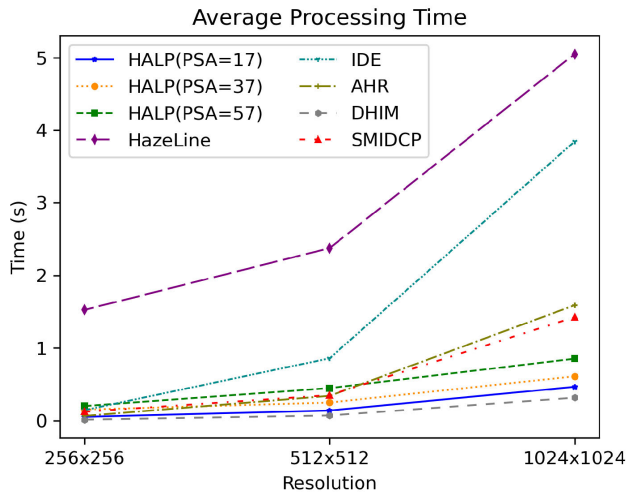


FIGURE 15. The visual comparison of the average processing time of different algorithms dehazing for images with different resolutions. The meaning of ‘PSA’ is the same as that in Table 4. For a clear view, we only plot the methods implemented on Matlab.

have very low computational latency and increase slowly with the improvement of image resolution.

C. THE KERNEL SIZE OF THE SIDE WINDOW FILTER

In this paper, the side window filter is introduced into the transmission estimation, which plays a significant role in dehazing. As an image filtering technique, the size of the filtering kernel often has an impact on the filtering result. Here we discuss the relationship between side window filters with different filter sizes and the dehazing performance of the proposed HALP. We set the side window filter size in the HALP algorithm as 5, 9, 17, 23, 29, 35, 41, 49, and 57, respectively, and then dehaze for samples on the RICE dataset [38]. The average PSNR, SSIM, and CIEDE2000 scores of the restored images are plotted in Fig. 16. The scores of PSNR and SSIM gradually improve as the filter size increases, because with the growth of patch size, the confidence of the dark channel prior increases.

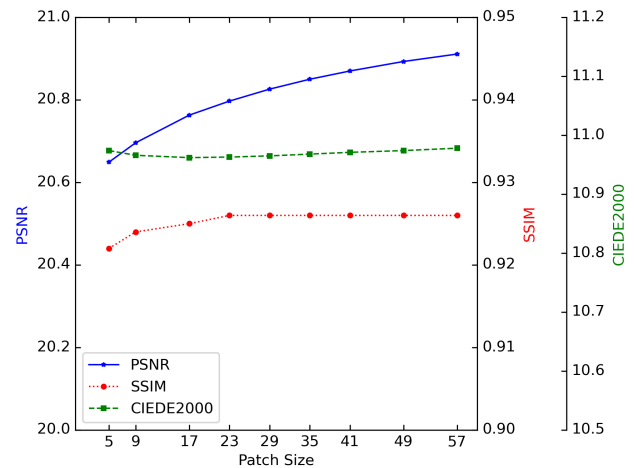


FIGURE 16. The full-reference assessment score curves of the HALP with different kernel size of the side window filter dehaizing on RICE dataset.

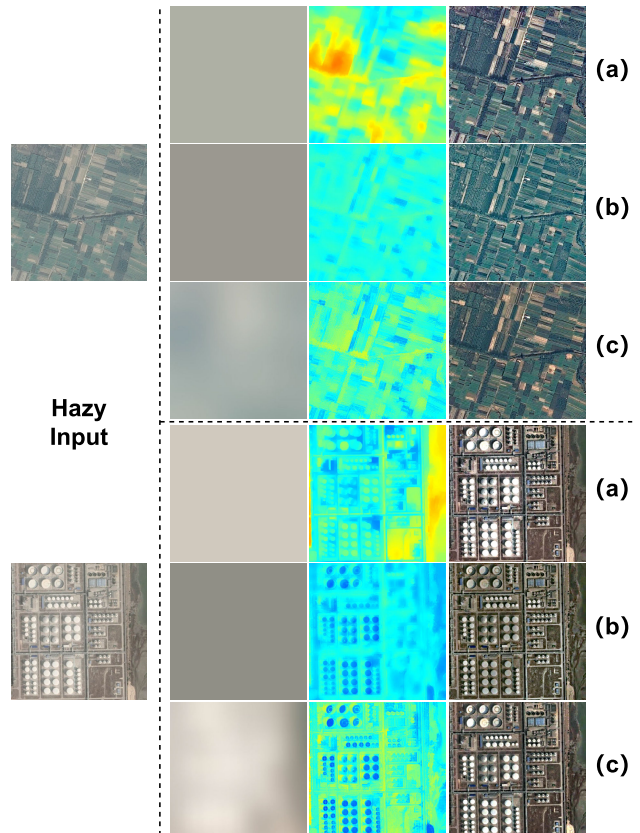


FIGURE 17. Visual comparison of the intermediate results. (a) HazeLine [5], (b) SMIDCP [9], (c) the proposed HALP. The two haze images on the left side of the dashed line are test samples from datasets AID [35] and DIOR [36], respectively. The three columns on the right side of the dashed line, from left to right, are the atmospheric light, transmission map, and dehazed results calculated by three test algorithms, respectively.

D. VISUAL COMPARISON OF THE INTERMEDIATE RESULTS

In addition to the quantitative analysis, to demonstrate the effectiveness of the proposed atmospheric light and transmission estimation methods, we visualize the intermediate results of the haze removal, as shown in Fig. 17. Compared



FIGURE 18. Haze removal for natural scene images. The top and bottom rows are haze images and restored results by the proposed method, respectively.

with other dehazing algorithms that take the single color from a particular pixel or a specific region in the input image as the global atmospheric light, atmospheric light of the HALP method is globally non-uniform calculated on each local image patch. Furthermore, the HALP algorithm retains more and sharper edge information in the transmission by the side window filter. As a result, the presented method recovers a more realistic haze-free image with better visibility.

E. HAZE REMOVAL FOR NATURAL SCENE IMAGES

The heterogeneous atmospheric light prior proposed in this paper is also applicable to outdoor natural images taken near the ground. We adopt our method to remove haze for four challenging outdoor haze images commonly used in natural image dehazing task, and the results are shown in Fig. 18. As we can see, HALP does a good job of restoring the emergent grass and the sharp colors of the distant mountains in the last sample in the figure. Moreover, it can process images with a large sky area, for example, the first two samples in Fig. 18. The third sample in the figure demonstrates that it still works well for images taken at close range. We attribute its incredible dehazing results to the fact that the algorithm can estimate the distribution of atmospheric light more accurately.

VII. CONCLUSION

In this paper, we propose a heterogeneous atmospheric light prior and a corresponding atmospheric light estimation algorithm, which can effectively cope with the restoration of the degraded remote sensing images. Then, we analyze the defects of the transmission estimation strategy in the DCP algorithm and adopt the side window filter technique to improve it without extra overhead. Finally, we compare our algorithm with a variety of existing algorithms on real-world remote sensing haze images. Experiments demonstrate that the proposed algorithm can dehaze well for remote sensing images with various haze scenes and obtains satisfactory results even in regular natural images. It should be noted that the proposed method relies on the reliability of the introduced heterogeneous atmospheric light prior, and when this prior is invalid, the algorithm may fail. Moreover, for extremely dense haze, the dehazing effect of the algorithm is limited. In future work, we will try to explore more robust priors for

haze image restoration, and try to fuse additional spectral information to obtain satisfactory dehazing results for dense haze cases.

REFERENCES

- [1] K. He, J. Sun, and X. Tang, “Single image haze removal using dark channel prior,” *IEEE Trans. Pattern Anal. Mach. Intell.*, vol. 33, no. 12, pp. 2341–2353, Dec. 2010.
- [2] R. Fattal, “Dehazing using color-lines,” *ACM Trans. Graph.*, vol. 34, no. 1, pp. 1–14, Dec. 2014.
- [3] Q. Zhu, J. Mai, and L. Shao, “A fast single image haze removal algorithm using color attenuation prior,” *IEEE Trans. Image Process.*, vol. 24, no. 11, pp. 3522–3533, Nov. 2015.
- [4] T. M. Bui and W. Kim, “Single image dehazing using color ellipsoid prior,” *IEEE Trans. Image Process.*, vol. 27, no. 2, pp. 999–1009, Feb. 2018.
- [5] D. Berman, T. Treibitz, and S. Avidan, “Single image dehazing using haze-lines,” *IEEE Trans. Pattern Anal. Mach. Intell.*, vol. 42, no. 3, pp. 720–734, Mar. 2020.
- [6] F. Xie, J. Chen, X. Pan, and Z. Jiang, “Adaptive haze removal for single remote sensing image,” *IEEE Access*, vol. 6, pp. 67982–67991, 2018.
- [7] X. Pan, F. Xie, Z. Jiang, and J. Yin, “Haze removal for a single remote sensing image based on deformed haze imaging model,” *IEEE Signal Process. Lett.*, vol. 22, no. 10, pp. 1806–1810, Oct. 2015.
- [8] L. Xu, D. Zhao, Y. Yan, S. Kwong, J. Chen, and L. Y. Duan, “IDeRs: Iterative dehazing method for single remote sensing image,” *Inf. Sci.*, vol. 489, pp. 50–62, Jul. 2019.
- [9] J. Li, Q. Hu, and M. Ai, “Haze and thin cloud removal via sphere model improved dark channel prior,” *IEEE Geosci. Remote Sens. Lett.*, vol. 16, no. 3, pp. 472–476, Mar. 2019.
- [10] Q. Liu, X. Gao, L. He, and W. Lu, “Haze removal for a single visible remote sensing image,” *Signal Process.*, vol. 137, pp. 33–43, Aug. 2017.
- [11] H. Shen, C. Zhang, H. Li, Q. Yuan, and L. Zhang, “A spatial-spectral adaptive haze removal method for visible remote sensing images,” *IEEE Trans. Geosci. Remote Sens.*, vol. 58, no. 9, pp. 6168–6180, Sep. 2020.
- [12] B. Cai, X. Xu, K. Jia, C. Qing, and D. Tao, “DehazeNet: An end-to-end system for single image haze removal,” *IEEE Trans. Image Process.*, vol. 25, no. 11, pp. 5187–5198, Nov. 2016.
- [13] W. Ren, S. Liu, H. Zhang, J. Pan, X. Cao, and M.-H. Yang, “Single image dehazing via multi-scale convolutional neural networks,” in *Proc. Eur. Conf. Comput. Vis.*, Cham, Switzerland: Springer, 2016, pp. 154–169.
- [14] B. Li, X. Peng, Z. Wang, J. Xu, and D. Feng, “AOD-Net: All-in-one dehazing network,” in *Proc. IEEE Int. Conf. Comput. Vis. (ICCV)*, Oct. 2017, pp. 4770–4778.
- [15] W. Ren, L. Ma, J. Zhang, J. Pan, X. Cao, W. Liu, and M.-H. Yang, “Gated fusion network for single image dehazing,” in *Proc. IEEE/CVF Conf. Comput. Vis. Pattern Recognit.*, Jun. 2018, pp. 3253–3261.
- [16] H. Dong, J. Pan, L. Xiang, Z. Hu, X. Zhang, F. Wang, and M.-H. Yang, “Multi-scale boosted dehazing network with dense feature fusion,” in *Proc. IEEE/CVF Conf. Comput. Vis. Pattern Recognit. (CVPR)*, Jun. 2020, pp. 2157–2167.
- [17] D. Chen, M. He, Q. Fan, J. Liao, L. Zhang, D. Hou, L. Yuan, and G. Hua, “Gated context aggregation network for image dehazing and deraining,” in *Proc. IEEE Winter Conf. Appl. Comput. Vis. (WACV)*, Jan. 2019, pp. 1375–1383.
- [18] B. Li, “Benchmarking single-image dehazing and beyond,” *IEEE Trans. Image Process.*, vol. 28, no. 1, pp. 492–505, Jan. 2019.
- [19] Z. Gu, Z. Zhan, Q. Yuan, and L. Yan, “Single remote sensing image dehazing using a prior-based dense attentive network,” *Remote Sens.*, vol. 11, no. 24, p. 3008, Dec. 2019.
- [20] A. Hu, Z. Xie, Y. Xu, M. Xie, L. Wu, and Q. Qiu, “Unsupervised haze removal for high-resolution optical remote-sensing images based on improved generative adversarial networks,” *Remote Sens.*, vol. 12, no. 24, p. 4162, Dec. 2020.
- [21] R. T. Tan, “Visibility in bad weather from a single image,” in *Proc. IEEE Conf. Comput. Vis. Pattern Recognit.*, Jun. 2008, pp. 1–8.
- [22] A. Khmag, S. A. R. Al-Haddad, A. R. Ramli, and B. Kalantar, “Single image dehazing using second-generation wavelet transforms and the mean vector L2-norm,” *Vis. Comput.*, vol. 34, no. 5, pp. 675–688, May 2018.

- [23] Z. Zhu, H. Wei, G. Hu, Y. Li, G. Qi, and N. Mazur, "A novel fast single image dehazing algorithm based on artificial multiexposure image fusion," *IEEE Trans. Instrum. Meas.*, vol. 70, pp. 1–23, 2021.
- [24] M. Zheng, G. Qi, Z. Zhu, Y. Li, H. Wei, and Y. Liu, "Image dehazing by an artificial image fusion method based on adaptive structure decomposition," *IEEE Sensors J.*, vol. 20, no. 14, pp. 8062–8072, Jul. 2020.
- [25] Z. Zhu, Y. Luo, H. Wei, Y. Li, G. Qi, N. Mazur, Y. Li, and P. Li, "Atmospheric light estimation based remote sensing image dehazing," *Remote Sens.*, vol. 13, no. 13, p. 2432, Jun. 2021.
- [26] C. Li, Y. He, and X. Li, "Feature attention parallel aggregation network for single image haze removal," *IEEE Access*, vol. 10, pp. 15322–15335, 2022.
- [27] X. Liu, Y. Ma, Z. Shi, and J. Chen, "GridDehazeNet: Attention-based multi-scale network for image dehazing," in *Proc. IEEE/CVF Int. Conf. Comput. Vis. (ICCV)*, Oct. 2019, pp. 7314–7323.
- [28] A. Mehta, H. Sinha, M. Mandal, and P. Narang, "Domain-aware unsupervised hyperspectral reconstruction for aerial image dehazing," in *Proc. IEEE Winter Conf. Appl. Comput. Vis. (WACV)*, Jan. 2021, pp. 413–422.
- [29] Y. Li and X. Chen, "A coarse-to-fine two-stage attentive network for haze removal of remote sensing images," *IEEE Geosci. Remote Sens. Lett.*, vol. 18, no. 10, pp. 1751–1755, Oct. 2021.
- [30] E. J. McCartney, *Optics of the Atmosphere: Scattering by Molecules and Particles*, vol. 1. New York, NY, USA: Wiley, 1976, p. 408.
- [31] S. G. Narasimhan and S. K. Nayar, "Interactive (de) weathering of an image using physical models," in *Proc. IEEE Workshop Color Photometric Methods Comput. Vis.*, vol. 6, Oct. 2003, p. 1.
- [32] S. G. Narasimhan and S. K. Nayar, "Vision and the atmosphere," *Int. J. Comput. Vis.*, vol. 48, no. 3, pp. 233–254, 2002.
- [33] H. Yin, Y. Gong, and G. Qiu, "Side window filtering," in *Proc. IEEE/CVF Conf. Comput. Vis. Pattern Recognit. (CVPR)*, Jun. 2019, pp. 8758–8766.
- [34] M. Ju, C. Ding, W. Ren, Y. Yang, D. Zhang, and Y. J. Guo, "IDE: Image dehazing and exposure using an enhanced atmospheric scattering model," *IEEE Trans. Image Process.*, vol. 30, pp. 2180–2192, 2021.
- [35] G.-S. Xia, "AID: A benchmark data set for performance evaluation of aerial scene classification," *IEEE Trans. Geosci. Remote Sens.*, vol. 55, no. 7, pp. 3965–3981, Jul. 2016.
- [36] K. Li, G. Wan, G. Cheng, L. Meng, and J. Han, "Object detection in optical remote sensing images: A survey and a new benchmark," *ISPRS J. Photogramm. Remote Sens.*, vol. 159, pp. 296–307, Jan. 2020.
- [37] B. Huang, Z. Li, C. Yang, F. Sun, and Y. Song, "Single satellite optical imagery dehazing using SAR image prior based on conditional generative adversarial networks," in *Proc. IEEE Winter Conf. Appl. Comput. Vis. (WACV)*, Mar. 2020, pp. 1806–1813.
- [38] D. Lin, G. Xu, X. Wang, Y. Wang, X. Sun, and K. Fu, "A remote sensing image dataset for cloud removal," 2019, *arXiv:1901.00600*.
- [39] A. Mittal, R. Soundararajan, and A. C. Bovik, "Making a 'completely blind' image quality analyzer," *IEEE Signal Process. Lett.*, vol. 20, no. 3, pp. 209–212, Mar. 2012.
- [40] A. Mittal, A. K. Moorthy, and A. C. Bovik, "No-reference image quality assessment in the spatial domain," *IEEE Trans. Image Process.*, vol. 21, no. 12, pp. 4695–4708, Dec. 2012.
- [41] L. K. Choi, J. You, and A. C. Bovik, "Referenceless prediction of perceptual fog density and perceptual image defogging," *IEEE Trans. Image Process.*, vol. 24, no. 11, pp. 3888–3901, Nov. 2015.
- [42] X. Pan, F. Xie, Z. Jiang, Z. Shi, and X. Luo, "No-reference assessment on haze for remote-sensing images," *IEEE Geosci. Remote Sens. Lett.*, vol. 13, no. 2, pp. 1855–1859, Dec. 2016.
- [43] Z. Wang, A. C. Bovik, H. R. Sheikh, and E. P. Simoncelli, "Image quality assessment: From error visibility to structural similarity," *IEEE Trans. Image Process.*, vol. 13, no. 4, pp. 600–612, Apr. 2004.



YUFENG HE (Member, IEEE) was born in 1991. He received the B.S. degree from Central South University, China, in 2014, and the M.S. degree from Hunan University, China, in 2020. He is currently an Assistant Professor with the College of Information Engineering, Tarim University, China. His research interests include computer vision and image processing.



CUILI LI (Member, IEEE) was born in 1991. She received the B.S. and M.S. degrees from China Agriculture University, China, in 2014 and 2016, respectively. She is currently an Assistant Professor with the College of Information Engineering, Tarim University, China. Her research interests include artificial intelligence, computer vision, image processing, and their applications in agriculture.



XU LI is currently a Professor with the Department of Computer Science, College of Information Engineering, Tarim University, China, where he is engaged in teaching and research work. His main research interests include remote sensing image processing and agricultural engineering.

• • •